



Characterization and Integrated Fabrication of Al Components with Thick TiC_p/Al Composite Coatings via Self-Propagating Reaction

Cunguang Chen, Tao Shi, Wenwen Wang, Zhimeng Guo, and Alex A. Volinsky

(Submitted January 14, 2019; in revised form April 30, 2019; published online July 5, 2019)

A novel and quick process combining self-propagating reaction with vacuum-expendable pattern casting is presented to accomplish integrated preparation of millimeter-thick TiC_p/Al composite coatings on the Al substrate. Titanium and graphite powders were mixed with the polytetrafluoroethylene (PTFE) additive and pasted on the expendable polystyrene (EPS) followed by compaction. Al components with in situ TiC_p/Al composite coating were simultaneously synthesized at a relatively low temperature of molten Al, which was poured into the assembly of EPS and powder compact inside the silica sands. Differential scanning calorimetry, x-ray diffraction, scanning electron microscopy with energy-dispersive spectroscopy and transmission electron microscopy were used to systematically investigate the thermodynamic characteristics of the reaction, the phase constituents, microstructure and tribological properties of the coatings. The infiltration model describing the densification of the reaction coatings was also developed for the critical wetting condition. The wear characteristics were assessed using a pin-on-disk tribometer with various loads. Results showed that uniform TiC particles stimulated by the PTFE-activated self-propagating reaction afforded superior mechanical properties and wear resistance.

Keywords coating, in situ TiC_p , microstructure, self-propagating reaction, wear resistance

1. Introduction

Aluminum components have a lot of advantages, such as high ductility, specific strength and low price, and are widely used in different applications in automobile, aircraft and other structural applications. However, the drawbacks of the low hardness and poor wear resistance accelerate the failure and shorten the service life of aluminum components (Ref 1). For improving the mechanical, tribological and chemical properties of aluminum components, various approaches, such as hypersonic flame spraying (Ref 2), plasma spraying (Ref 3, 4), laser cladding (Ref 5, 6) and micro-arc oxidation (Ref 7-9), have been developed to synthesize the coatings on the surface of aluminum components. Meanwhile, aluminum matrix composite (AMC) layers with interesting properties and very good adhesion to the aluminum substrate have been prepared by a selection of the suitable combination of metallic substrate and ceramic particles. In general, these AMC coatings can only be used for surface reconstruction. The above fabrication techniques are difficult to implement for the integrated formation of

net-shape aluminum components with AMC coatings, except for low production efficiency, thin coatings (from a few to dozens of microns) and poor adhesive strength between the coatings and the aluminum substrate.

AMC components can be produced with the net-shape and near-net shape by numerous methods, such as stir casting (Ref 10, 11), squeeze casting (Ref 12, 13), melt infiltration (Ref 14, 15) and powder metallurgy (Ref 16, 17). In many cases, it is not necessary to have the properties of AMCs for the whole structural component, for instance, when the primary requirements are high surface hardness and good wear resistance. In this case, AMC layers need to be strongly bonded to aluminum components in order to simultaneously meet the design objectives of cost and weight efficiency.

Considering the self-propagating high-temperature synthesis (SHS) as an increasingly prevalent technology for manufacturing of in situ surface composite coatings (Ref 18-22), an intriguing process, i.e., SHS combined with the vacuum-expendable pattern casting (V-EPC) (Ref 23, 24), has been utilized to integrally synthesize the components with coatings consisting of metallic matrix composites reinforced with ceramic particles. The V-EPC is regarded to be easily adaptable and economically viable due to its low processing cost and high production rate. The V-EPC is also an attractive processing method since it offers a wide selection of structures and materials. On the one hand, the shape and structure of the expendable patterns are freely designed and processed by the numerical control equipment. On the other hand, the expendable pattern is usually polystyrene that decomposes easily when heated even to low temperatures. The authors have developed a unique technique combining the SHS with the V-EPC to fabricate in situ TiC/Cu (Ref 25) and $\text{TiC}-(\text{Cr,Fe})_7\text{C}_3/\text{steel}$ (Ref 26) composite coatings with a controllable thickness on copper and high manganese steel substrates. The SHS reaction can be accomplished spontaneously when the metallic melt above

Cunguang Chen and Zhimeng Guo, Institute for Advanced Materials and Technology, University of Science and Technology Beijing, Beijing 100083, China; Tao Shi, GRIPM Advanced Materials Co. Ltd, Beijing 101407, China; Wenwen Wang, School of Mathematics and Physics, University of Science and Technology Beijing, Beijing 100083, China; and Alex A. Volinsky, Department of Mechanical Engineering, University of South Florida, Tampa, FL 33620. Contact e-mails: cgchen@ustb.edu.cn and volinsky@usf.edu.

1000 °C infiltrates into the porous reaction system. This realizes quick preparation within a few minutes; thus, the process is promising for scaled-up production of composite components in a simple and economical way.

However, the integrated preparation of aluminum components with AMC coating via the SHS process combined with the V-EPC is a challenge due to difficulty in overcoming the activation energy barrier of the SHS reaction at a relatively low temperature of molten aluminum. Fortunately, investigations for overcoming this problem, which would result in the ignition of the SHS reaction by the molten aluminum by introducing polytetrafluoroethylene (PTFE) as the reaction activator, are thus valuable and make the integrated production of the AMC coating and aluminum substrate more promising (Ref 27-30). In addition, as for choosing reinforcements, TiC particulate (TiC_p)-reinforced AMCs are very interesting because TiC particles are thermodynamically stable and enhance the hardness of the composite, making it a promising candidate for wear-resistant components (Ref 31). Furthermore, the Ti-C system is comparatively mature in the SHS reaction and good wettability between the TiC ceramic phase and the liquid aluminum matrix has been demonstrated for generating satisfactory bonding during casting (Ref 32, 33).

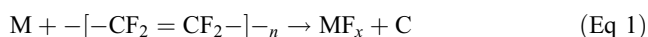
Therefore, based on the novel and efficient process of the SHS plus V-EPC proposed in this paper, the microstructure, mechanical properties and wear behavior of the surface composite coatings were investigated aiming at integrally fabricating aluminum components with millimeter-level TiC_p/Al composite coating. Also, the influence of in situ TiC particle size on the infiltration process of liquid aluminum was addressed under the critical condition of wetting. It is expected that these meaningful results are significant for promoting the development and practical applications of surface composite coatings on the large-size aluminum components.

2. Experimental Procedure

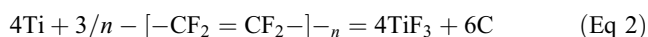
2.1 Experimental Principles

In this work, the SHS reaction of the Ti-C system is expected to be induced by the molten aluminum during casting. However, the temperature and heat of the aluminum melt are too low to overcome the activation energy barrier, resulting in the incapable SHS reaction. To solve this problem, the promoter, PTFE, should be added to the initial mixture to guarantee that the SHS reaction of the Ti-C system can be successfully triggered. Cudziło et al. (Ref 34) calculated the adiabatic temperature (T_{ad}) of the Ti-PTFE system, and the

results showed that it was much higher than 1,800 K, so that the SHS reaction could be realized with 10-90 wt.% Ti. The decomposition of PTFE is supposed to occur at the aluminum melting temperature, and then the reaction between metallic elements (M) and PTFE could be expressed as:



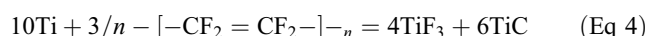
The reaction is exothermic and the amount of heat is high enough to ignite the SHS reaction. Besides, the MF_x product is gaseous during the SHS, which means that it could be easily extracted under vacuum during the V-EPC process. In this study, the reaction between Ti and PTFE is:



The product C can react with Ti according to the following reaction:



In conclusion, the whole reaction can be written as:



Consequently, the mixture of Ti and PTFE (further marked as TP) with the ratio of reaction (4) was chosen as the promoter for the Ti-C SHS system in this study.

2.2 Raw Materials

The matrix material of the surface composite was pure aluminum from refined aluminum ingots (Al, 99.9% purity, Beijing Trillion Metals Co., Ltd.). Commercially available powders of titanium (Ti, 99.7% purity, ~45 μm, Tech-Long Metal Materials Co., Ltd., Tianjin), graphite (C, 99.5% purity, ~10 μm, Tianjin Wanhe Tianyi Technology Co., Ltd.) and granulated PTFE with analytical purity (Tianjin Wanhe Tianyi Technology Co., Ltd.) were obtained.

2.3 Preparation Process

Raw powders of Ti and C were weighted according to the stoichiometry of the SHS reaction. For the TP mixture, Ti and PTFE were measured based on reaction (4). Powders were mixed for 2 h using a centrifugal mill. The composition of the powder mixture is listed in Table 1. The mixed powders were compacted at 160 MPa to the 40 mm × 40 mm × 4 mm size to obtain 70 ± 2% of the theoretical full density and then were pasted on the 40 mm × 40 mm × 20 mm EPS surface. They were dried together at 50 °C for 2 h and placed into the silica sand after the fireproof coating was brushed off. Small aluminum blocks were smelted in a medium-frequency induction furnace and cast under negative pressure (−0.03 MPa to

Table 1 The composition of the powder mixtures

Sample	Composition	Mass fraction of TP, wt.%	Mass fraction of corresponding PTFE, wt.%
0	Ti+C	0	0
1	Ti+C+TP	5	1.9
2	Ti+C+TP	10	3.8
3	Ti+C+TP	15	5.8
4	Ti+C+TP	20	7.7
5	Ti+C+TP	30	11.5

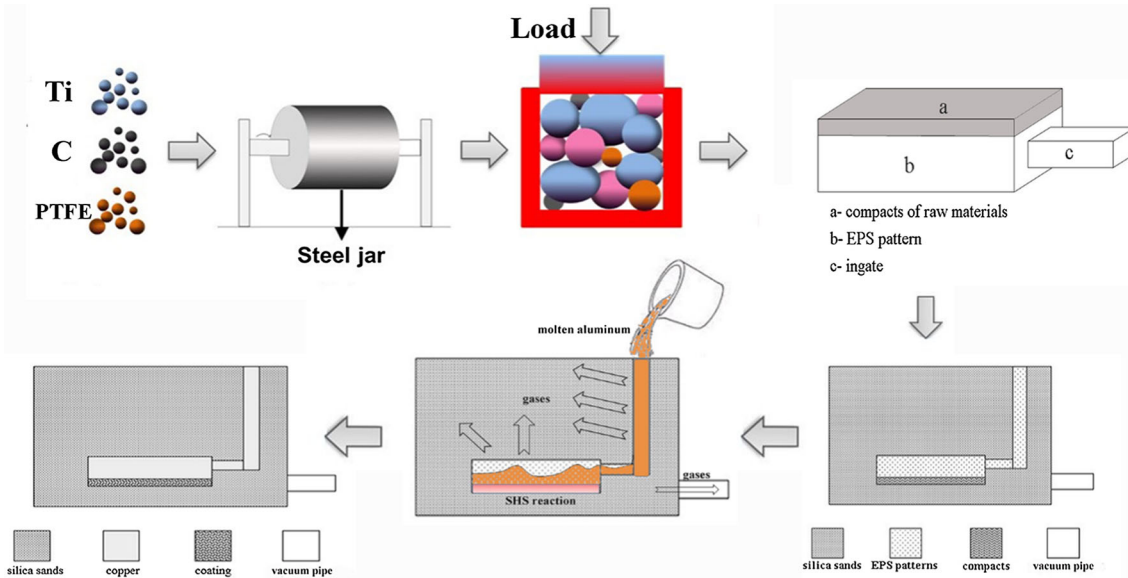


Fig. 1 Schematics of the surface composite coating process

–0.04 MPa) when the temperature of molten aluminum reached 780 °C. The in situ TiC_p surface composite coating was synthesized simultaneously with aluminum solidification. The schematic diagram of the fabrication process is shown in Fig. 1.

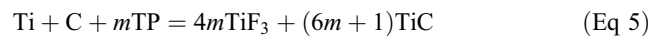
2.4 Characterization and Measurements

Differential scanning calorimetry (DSC) of TP (Ti-PTFE), Ti-C and Ti-C-TP was conducted using the DSC-TGA Q Series instrument (SDT Q600). For phase identification, an x-ray diffractometer (XRD) was used with Cu $K\alpha$ radiation (1.54 Å) generated at 40 kV and 150 mA. A scanning electron microscope (SEM, LEO 1450) equipped with energy-dispersive spectroscopy (EDS) was used for microstructure characterization. A transmission electron microscope (TEM, Tecnai G2 F30) was used to clearly demonstrate the presence and characterize in situ TiC particles. Vickers hardness measurements of the coatings were carried out using a hardness testing machine (LEICA VMHT30M) under 50 g load. Wear tests were performed using a pin-on-disk tribometer to determine the weight loss with respect to time. The equipment was composed of a sample holder and a rotating disk with 600# SiC sandpaper on the surface. The speed of the rotating disk was maintained at 1380 mm/s, and normal loads of 10 N, 15 N and 20 N were applied to the sample. These tests were carried out on $\Phi 10 \text{ mm} \times 15 \text{ mm}$ coated coupons for 20 min. X-ray photoelectron spectroscopy (AXIS ULTRA^{DLD} with Al $K\alpha$ x-ray source) was used to characterize the chemical states of the worn surface of the in situ TiC_p/Al composite coating. C 1s and Ti 2p peaks were recorded at high resolution.

3. Results and Discussion

3.1 Adiabatic Temperature and DSC Analysis

Following reaction (4), the Ti-C-TP system reaction can be written as:



Here, m is the molar quantity of TP. Based on the empirical criterion proposed by Merzhanov et al. (Ref 35), the SHS reaction would not self-sustain when T_{ad} is lower than 1,800 K. The T_{ad} value of the Ti-C-TP system can be calculated as follows:

$$\begin{aligned} & (6m + 1)\Delta H_{f,298,\text{TiC}}^\ominus + 4m\Delta H_{f,298,\text{TiF}_3}^\ominus \\ & + (6m + 1) \int_{298}^{T_{\text{ad}}} C_p(\text{TiC})dT + 4m \int_{298}^{T_{\text{ad}}} C_p(\text{TiF}_3)dT \\ & = 0 \end{aligned} \quad (\text{Eq } 6)$$

Here, ΔH_f^\ominus is the standard state enthalpy at 298 K, and C_p is the molar heat capacity. Figure 2 presents the T_{ad} values as a function of the mass fraction (w) of TP, which could be deduced from Eq 7 based on the TP molar quantity (m) in the Ti-C-TP system:

$$w = \frac{m(10M_{\text{Ti}} + 3M_{\text{C}_2\text{F}_4})}{M_{\text{Ti}} + M_{\text{C}} + m(10M_{\text{Ti}} + 3M_{\text{C}_2\text{F}_4})} \times 100\% \quad (\text{Eq } 7)$$

Here, M is the molecular weight of each component above. It could be seen from the calculated results that the Ti-C-TP system reaction was highly exothermic, and the T_{ad} of the system was much higher than 1,800 K with the addition of 0-40 wt.% TP mixture. Therefore, once the reaction of the Ti-C-TP system was ignited, the whole self-spreading process was undoubtedly accomplished. Besides, when the TP mixture was added, the overall T_{ad} decreased significantly. It could be explained that the reaction produced TiF_3 , which was in the gas form at the high temperature during the reaction and absorbed some of the released heat. At the same time, Ti may be melted due to the exothermic reaction, and some heat would be also absorbed. Hence, the T_{ad} of the Ti-C-TP system was lower than the Ti-C independent reaction.

DSC experiments for all mixed raw materials shown in Table 1 were carried out to demonstrate the effects of PTFE on the Ti-C SHS reaction, as illustrated in Fig. 3 and 4. The

thermal behavior of TP and Ti-C mixtures was studied by DSC (Fig. 3a and b). According to the DSC curve of the TP system (Fig. 3a), an exothermic effect was recorded at 470-550 °C caused by the reaction between Ti and PTFE. As for the Ti-C mixture (Fig. 3b), the main exothermic peak appeared at about 800 °C. The SHS reaction of Ti-C would not be ignited below this temperature.

The addition of different mass fractions of TP in the Ti-C mixture led to significant changes in the reactions shown in Fig. 4. When the TP content reached 5 and 10 wt.% (Fig. 4a and b), DSC curves had two exothermic peaks, which correspond to the reactions of TP and Ti-C, respectively. Increasing the TP content decreased the Ti-C exothermic peak intensity (Fig. 4c, d and e), while the TP peak intensity increased. As seen in this case, the heat released from the TP reaction could ignite the Ti-C SHS reaction. With the relatively high content of TP (30 wt.%), the SHS reaction of the Ti-C system could happen and finish under about 500 °C, approximately considered as the ignition temperature of TP.

3.2 Phases and Microstructure Observations

The mixture compacts, Samples 0 and 1, were peeled off from the surface of the aluminum casts after finishing the manufacturing process. The results showed that the heat of molten aluminum was too low to ignite the SHS reaction of the

Ti-C system, based on the analysis mentioned above. In spite of the addition of 5 wt.% TP, the heat released from the Ti-C-TP reaction was not enough to sustain the whole reaction self-propagation, considering the low heat and good thermal conductivity of molten aluminum.

Figure 5 presents the XRD patterns of the Samples 2-5. According to the XRD results, the TiC phase was present in all samples, which means that the PTFE addition could ignite the Ti-C SHS reaction under relatively low temperature. There were only two TiC and Al phases present in all coatings, indicating that the SHS reaction of the Ti-C system was completed. As predicted by Eq 2, TiF₃ was not detected in all these coatings. Under the action of negative pressure during the casting process, the gaseous TiF₃ product was extracted from the cavities of the sand mold with the liquefaction and gasification products of the EPS foam before the cast cooling. It should be noted that the TP system could be added as the activator or accelerator to ignite the Ti-C SHS reaction at lower temperatures. Once the reaction was ignited, it could be completely carried out to the end, consequently generating the SHS coating enhanced with TiC particles in the matrix of Al casts.

Typical backscattered electron images of the samples are shown in Fig. 6 and 7. With the increase in the PTFE content, the uniformity of the coating microstructure was changed. As the TP mixture content was increased from 10 wt.% (Sample 2) to 15 wt.% (Sample 3), the resulting enhanced phase particles were distributed more evenly, and the interface between the coating and the substrate was obvious, as seen in Fig. 6(a) and (b). However, when the TP content reached 20 wt.% (Sample 4), the uniformity of the coating microstructure began to deteriorate, and the interface is not clearly seen in Fig. 6(c). Furthermore, the hard particles were distributed in the top section of the cast Sample 5 with 30 wt.% TP in Fig. 6(d). These phenomena should be related to the high exothermic reaction of the TP system. If the TP content in the coating system was too high, it could cause a dramatic increase in the reaction extent and degassing, resulting in broken up product skeleton. As the infiltration of the Al liquid, the hard particles dissociated throughout the coating area, which showed inhomogeneous coating microstructure.

Figure 7 shows the microstructure of each coating of the Samples 2-5 at higher magnification. In view of the EDS analysis results in Table 2, it was obvious that the light phase corresponded to TiC, while the dark region was the aluminum matrix. The phases present in the coating were identified as the Al matrix constituent with in situ TiC particles. Interestingly, by

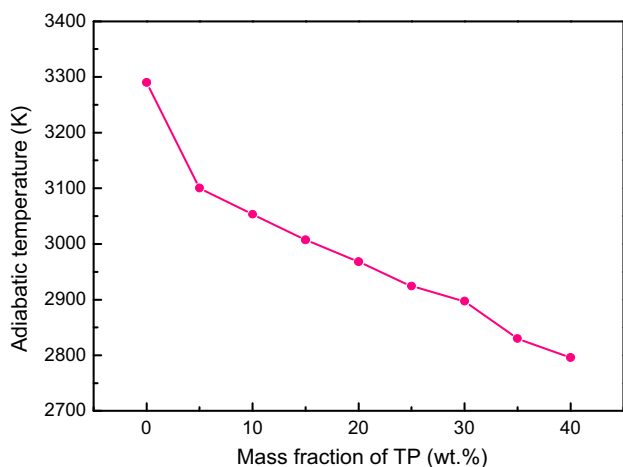


Fig. 2 Adiabatic temperature (T_{ad}) of the Ti-C-TP system as a function of the TP content

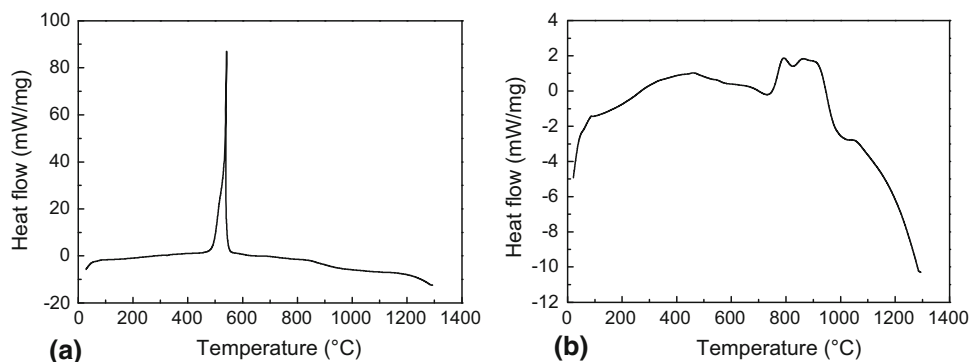


Fig. 3 DSC results of: (a) TP (Ti + PTFE) and (b) Ti-C systems

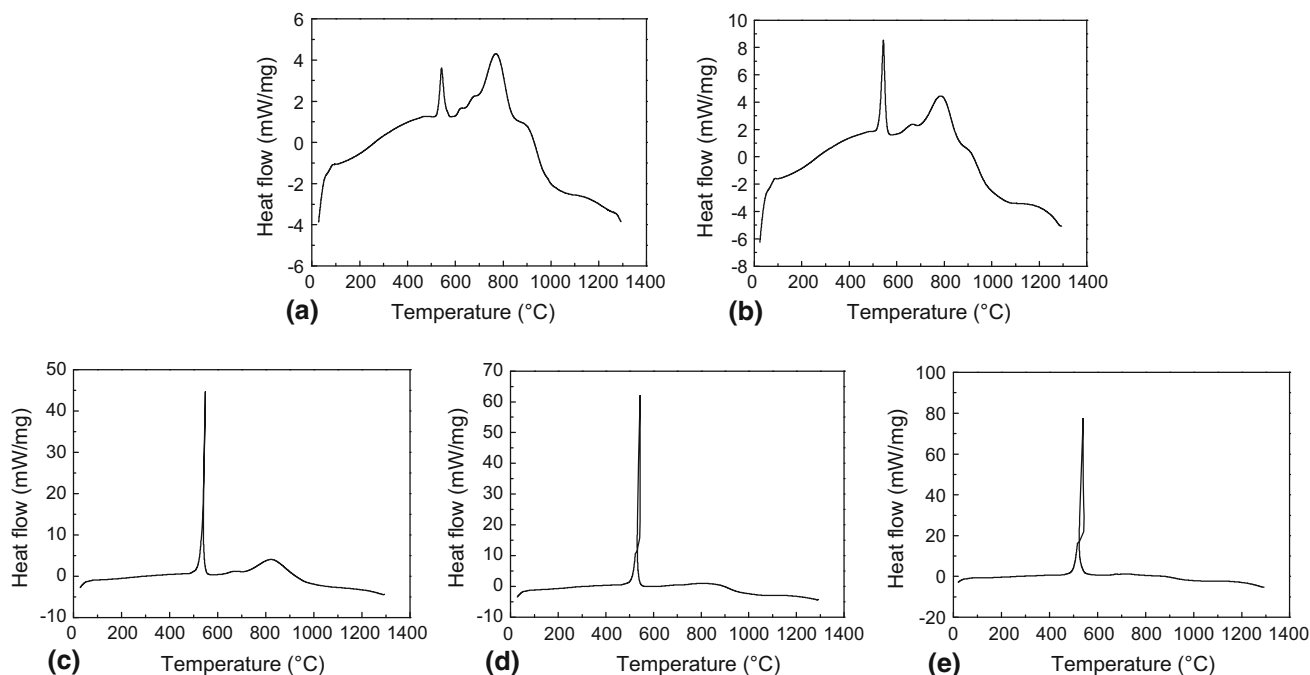


Fig. 4 DSC results of: (a) Ti-C + 5 wt.% TP, (b) Ti-C + 10 wt.% TP, (c) Ti-C + 15 wt.% TP, (d) Ti-C + 20 wt.% TP and (e) Ti-C + 30 wt.% TP

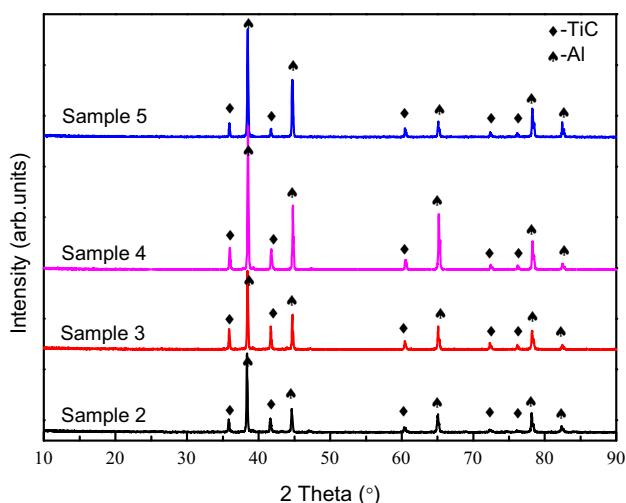


Fig. 5 XRD patterns of the Samples 2-5

microanalysis of the interface region in the cross section of the coated substrate of the Sample 3 in Fig. 8(a), it was found that the TiC_p/Al coating on the Al substrate formed sound joints without any obvious void defects. Furthermore, the EDS results in Fig. 8(b) were consistent with the XRD analysis in Fig. 5. It could be seen that the microstructure with the optimal distribution and 1-10 μm phase size is presented in Fig. 7(b) due to the 15 wt.% TP addition. Meanwhile, TEM observations in Fig. 9(a) revealed that the TiC particles were sub-spherical, and a good interface was formed with the Al matrix. Furthermore, the selected area electron diffraction (SAED) pattern in Fig. 9(b) showed that the in situ TiC particulates existed with the regular face-centered cubic crystal structure. In previous studies (Ref 36, 37), the formation mechanism of TiC

was proposed. For the different sizes of Ti and graphite particles, the TiC nucleated with fine graphite particles at the interface between solid Ti and liquid Ti phases saturated in graphite. The melted aluminum infiltrated after the combustion wave, and the coating densification was achieved via aluminum melt filling the pores produced by SHS. Besides, there were only TiC and Al matrix phases in the composite with fine graphite particles, and the SHS reaction would proceed to completion with fine graphite particles.

As for 10 wt.% TP, even though the heat released served to ignite the SHS reaction of the Ti-C system, the overall heat was relatively low, and some of the resulting TiC particles did not have enough time to be dispersed as the aluminum melt infiltrated and cooled down. Therefore, the microstructure with sub-spherical particles and bulk agglomerates was formed as seen in Fig. 7(a). Moreover, huge amounts of heat and gas were released with 20 and 30 wt.% TP. The generated TiC particles were thus scattered into uneven agglomerates in the matrix with the infiltration and solidification of the aluminum melt, leading to the formation of microstructure shown in Fig. 7(c) and (d).

3.3 Infiltration Process of Liquid Aluminum

Once the SHS reaction was ignited, the aluminum melt infiltrated into the pores of products with combustion wave and filled the pores. The densification of the coating was realized afterward. Since the aluminum melt did not participate in the SHS reaction, it could be regarded that the infiltration of aluminum melt and the SHS reaction were two separate processes. The driving force, P , which prompted the densification could be expressed as:

$$P = P_A + P_B + P_C + P_G \quad (\text{Eq 8})$$

Here, P_A is the negative pressure during casting, which is considered constant at -0.04 MPa. P_B is the static pressure of the aluminum melt in the pouring runner, $P_B = \rho gh$, where ρ is

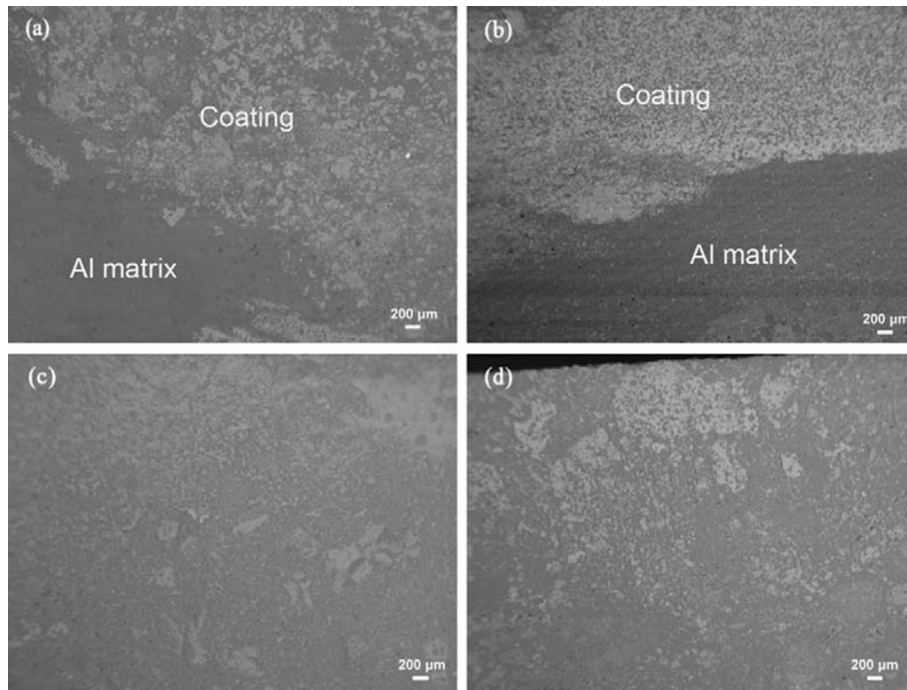


Fig. 6 SEM images of the cross section of representative coatings in: (a) Sample 2, (b) Sample 3, (c) Sample 4 and (d) Sample 5

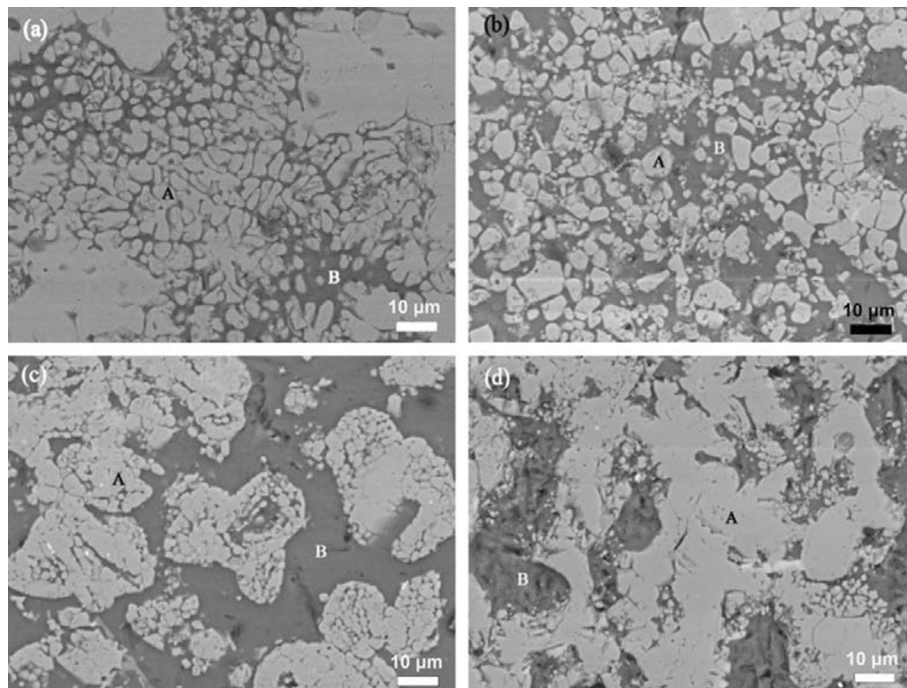


Fig. 7 High-magnification SEM images of the cross section of representative coatings in: (a) Sample 2, (b) Sample 3, (c) Sample 4 and (d) Sample 5

the density of the liquid aluminum, g is the gravitational acceleration, and h is the height of the liquid column of 400 mm. P_C is the capillary pressure. P_G is the gravitational pressure of the liquid aluminum, $P_G = \rho g l$, where l is the infiltration length equal to the 5 mm thickness of the compact. The capillary pressure, P_C , as described by the Laplace's law, could be written as:

$$P_C = \frac{2\gamma_{lv} \cos \theta}{r_c} \quad (\text{Eq 9})$$

Here, γ_{lv} is the surface tension, θ is the contact angle, and r_c is the capillary radius, $r_c = \frac{D_0 \varepsilon}{3\lambda(1-\varepsilon)}$, where D_0 is the average diameter of the particulate, ε is the void fraction of the powder compact, and λ is a geometric factor, which depends on the

geometry of both the capillary channel and the particulate. For non-spherical and angular particulates, as confirmed by Oh (Ref 38), the λ value was determined in experiments with perfect wetting liquids as 1.4.

Furthermore, the infiltration length–time relationship can be calculated using the following equation:

$$l^2 = \int \frac{r_c^2}{4\eta} [P_A + P_C + \rho g(h + l)] dt \quad (\text{Eq 10})$$

Here, η is the viscosity of liquid aluminum of 8.1×10^{-4} Pa s. Equation 10 is derived using Eq 8 and 9 and the Washburn relationship (Ref 39, 40). Considering the critical condition, an assumption of the contact angle, θ , was made as 89.9° when the liquid aluminum just came into contact with generated TiC particles. As seen from Fig. 7(b), the size of TiC

particles varied from 1 to 10 μm . Herein, the size of TiC was chosen as 5 μm and 10 μm to compare the effects of TiC particles on the infiltration process. Using Eq 10, the infiltration length–time relationship for the Ti-C-TP system can be plotted as shown in Fig. 10. The calculated results show that the infiltration is completed within a very short time (a few seconds), which matches well with the results of mass gain in the present work. In the critical condition, the larger the synthesized TiC particles, the faster the infiltration speed. When the infiltration length, l , was 5 mm, the infiltration time in the region of 10 μm TiC particles was about 1 s, and in the 5 μm TiC particles region it was about 3.7 s. When a combustion reaction occurred, the temperature of the compact increased due to exothermic heat generated by the reaction and accordingly, the contact angle, θ , would decrease to provide higher capillary pressure, P_C , which was the main driving force for spontaneous infiltration. Therefore, the melt could infiltrate spontaneously into the compact when the critical temperature was exceeded. This can account for the experimental observation that when coarser in situ TiC particles were produced, the V-EPC process was completed faster.

Table 2 EDS results of the light phase (A) and the dark region (B) in Fig. 6

Element	Mass fraction, wt.%							
	Sample 2		Sample 3		Sample 4		Sample 5	
	A	B	A	B	A	B	A	B
C	17.79	...	23.89	...	16.67	...	16.66	...
Ti	82.21	...	76.11	...	83.33	...	83.34	...
Al	...	100	...	100	...	100	...	100

3.4 Hardness

The microhardness was measured on a number of cross sections of each coating, as shown in Fig. 11. The standard deviation of every measurement was $\pm 5\%$. The microhardness measurements were carried out for each investigated composite at room temperature for 15 s under 50 g normal load. Because

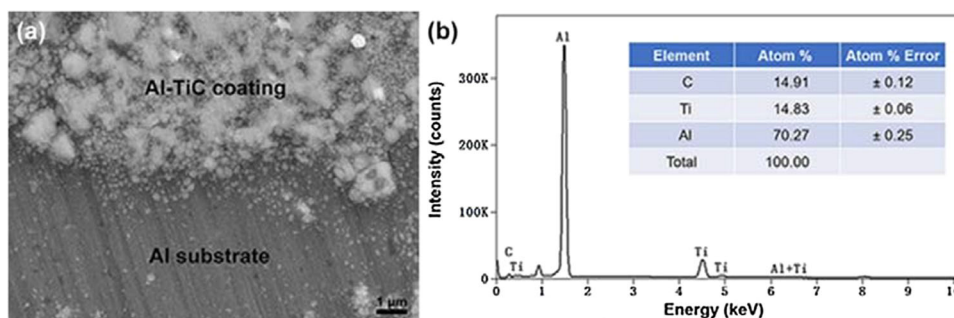


Fig. 8 Microanalysis of the interface region in the cross section of the coated substrate of the Sample 3: (a) interface microstructure and (b) EDS results

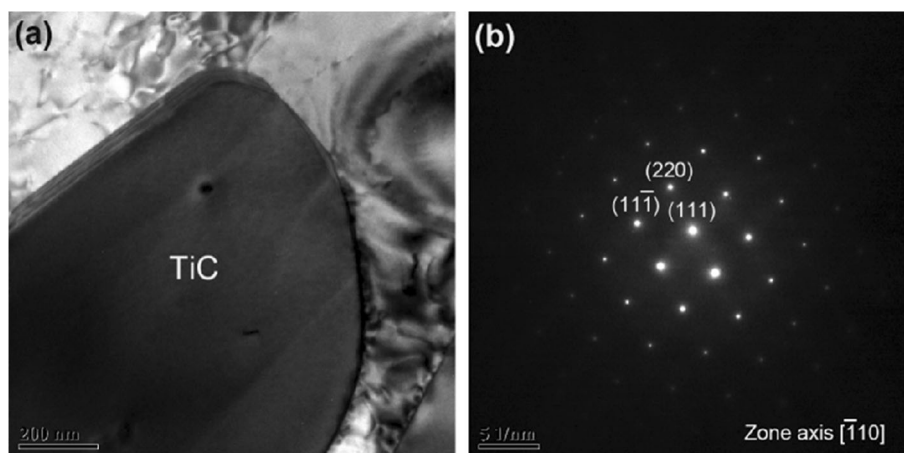


Fig. 9 TEM images of (a) the in situ TiC particle and (b) the corresponding SAED pattern

of the reinforcement effect of the TiC particles, the microhardness of the coatings was higher than the aluminum matrix ($\sim HV_{0.05} 40$). As for each microhardness curve of the Samples 2-4, the microhardness ascended first from the outer surface to the interior (~ 0.5 mm distance from the top), while the Sample 5 had no evident change. After that, the fluctuations of hardness happened until the distance from the top of the Samples 2 and 3 reached about 3.5 mm, and then the microhardness sharply declined. The hardness fluctuations depended on the coating microstructure shown in Fig. 6 and 7. Since the SHS product was porous, molten Al infiltrated into the pores, and the densification by solidification was completed with good bonding between the coating and the matrix. The distribution of hard phase particles was not entirely uniform, and thus, the hardness fluctuations existed. Regarding the Samples 4 and 5, the microhardness almost dropped linearly until the distance from the top reached about 4 mm and then was lowered to the same values as Samples 2 and 3 when the distance from the top was 5 mm. Therefore, it could be deduced that the thickness of the four samples coating prepared by the V-EPC with the SHS

was up to about 5 mm, which was the thickest coating of all reports on the surface strengthened layer of aluminum alloys.

Additionally, among the four samples, the Sample 3 with 15 wt.% TP had relatively higher hardness. More uniform hard particles distribution in the SHS coating resulted in higher hardness. This could be inferred from the even carbide distribution in the microstructure of the coating in the Sample 3. On the contrary, the higher TP content (20 and 30 wt.%) caused greater amounts of heat and gas released in the reaction system and hence lowered the hardness of the coating due to uneven TiC agglomerates, as seen from Fig. 7(c) and (d).

3.5 Wear Behavior

Figure 12 demonstrates the variation of weight loss for the four samples and the Al matrix by using a pin-on-disk tribometer under various loads (10 N, 15 N and 20 N). The wear resistance performance of all four samples is obviously superior to the aluminum matrix. The reduction of weight loss compared to the matrix could be attributed to the presence of the TiC reinforcement phase. At higher 20 N load the weight loss of each sample became relatively high. According to the hardness changes, the Sample 3 with 15 wt.% TP exhibited the best wear resistance compared to other samples, while the wear properties got worse with the increase in TP content to 20 and 30 wt.%.

Figure 13 shows the worn surfaces of the Samples 2-5 tested under various loads (10 N, 15 N and 20 N). The worn surfaces were characterized as long continuous grooves with a certain degree of plastic deformation. The low hardness of pure aluminum matrix could not effectively support the scratching and cutting of SiC abrasive particles in the sandpaper, and not providing strong support for keeping TiC particles in place. The surface morphology showed the plowing effect on the coatings. The plowing severity in Fig. 13(d)-(f) was partly less for the Sample 3 because the coating on the Sample 3 has the optimal performance in terms of the hardness and particles uniform distribution. With the load increase, the plowing in each sample became more severe and caused fast removal of material from the coating, leading to more weight loss.

For the composition and phase analysis of the worn surface on the Sample 3 at 15 N, x-ray photoelectron spectroscopy (XPS) was conducted to investigate the chemical bonding states

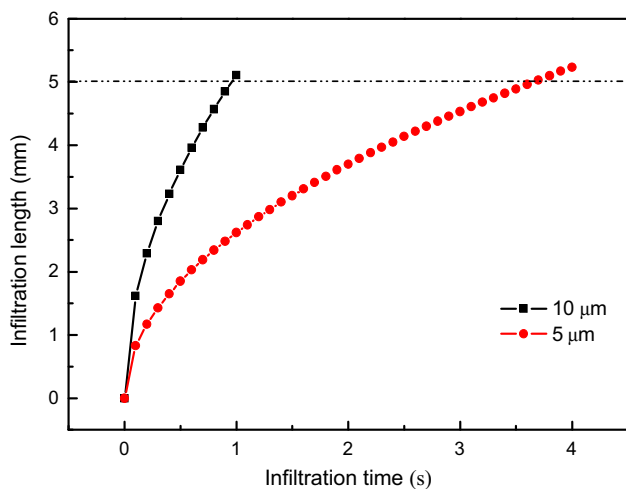


Fig. 10 Relationship between the infiltration length and time

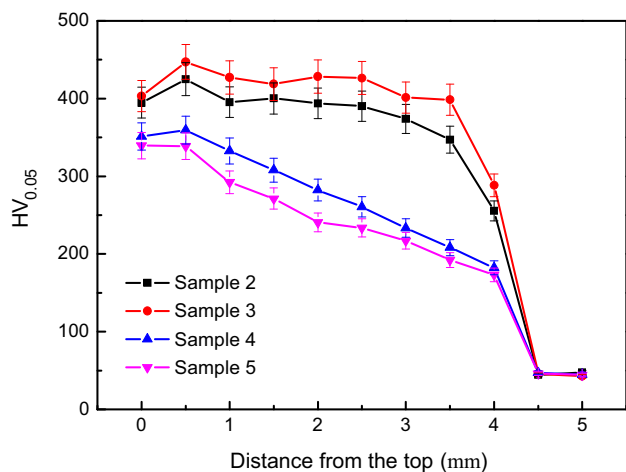


Fig. 11 Microhardness of the cross section of the corresponding coatings

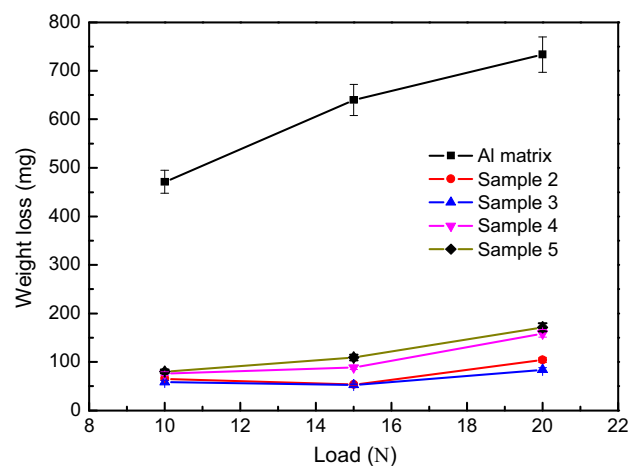


Fig. 12 Weight loss of the four samples and the Al matrix from the pin-on-disk wear tests

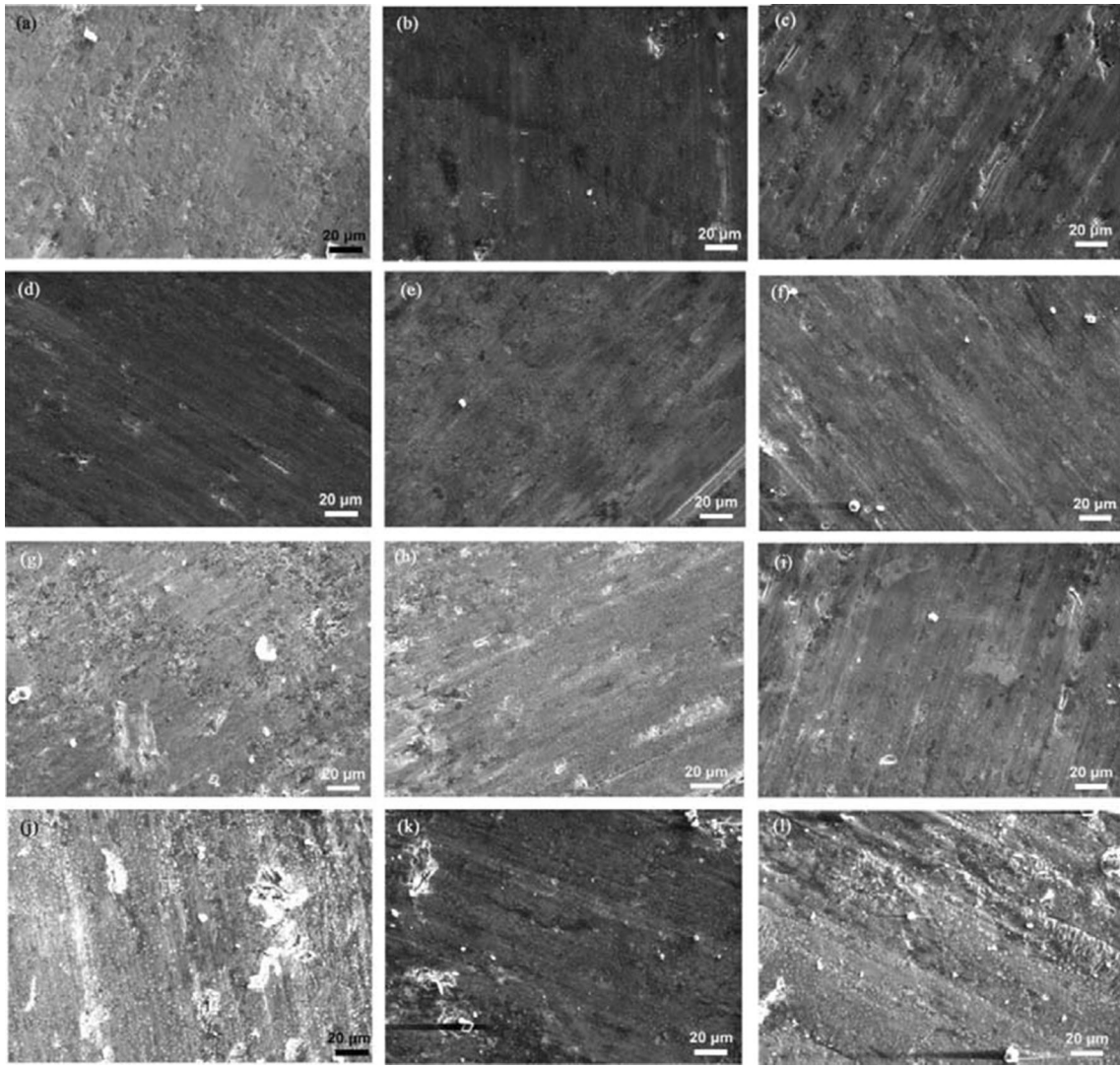


Fig. 13 SEM micrographs of wear surfaces on: (a) Sample 2 at 10 N, (b) Sample 2 at 15 N, (c) Sample 2 at 20 N, (d) Sample 3 at 10 N, (e) Sample 3 at 15 N, (f) Sample 3 at 20 N, (g) Sample 4 at 10 N, (h) Sample 4 at 15 N, (i) Sample 4 at 20 N, (j) Sample 5 at 10 N, (k) Sample 5 at 15 N and (l) Sample 5 at 20 N

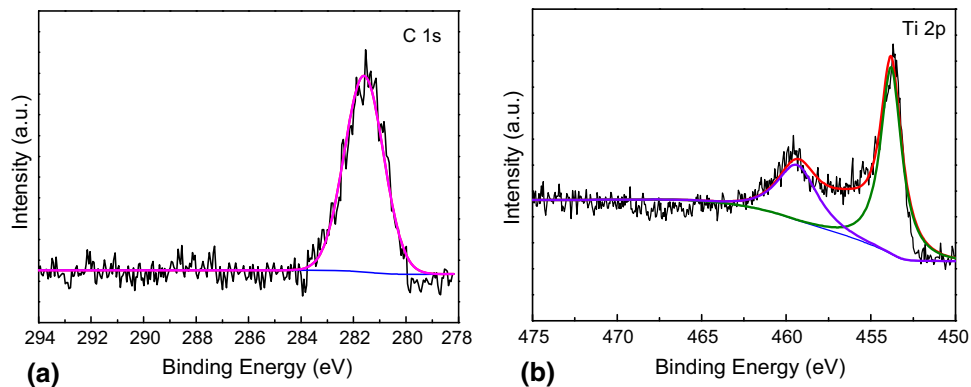


Fig. 14 XPS patterns of (a) C 1s and (b) Ti 2p of the worn surface on the Sample 3 at 15 N

within the compounds. Figure 14 displays the results of the XPS analysis for the C 1s and Ti 2p binding energies. Figure 14(a) shows the C 1s spectra of the composite coating. The C 1s peak of TiC is observed at 281.9 eV (Ref 41). The

peak of graphite is absent in the spectrum. The peaks at 454 eV and 460 eV were observed, corresponding to the Ti 2p spectra from the titanium carbide (Ref 25). Figure 15 shows the EDS mapping of the worn surface on the Sample 3 at 30 N. From the

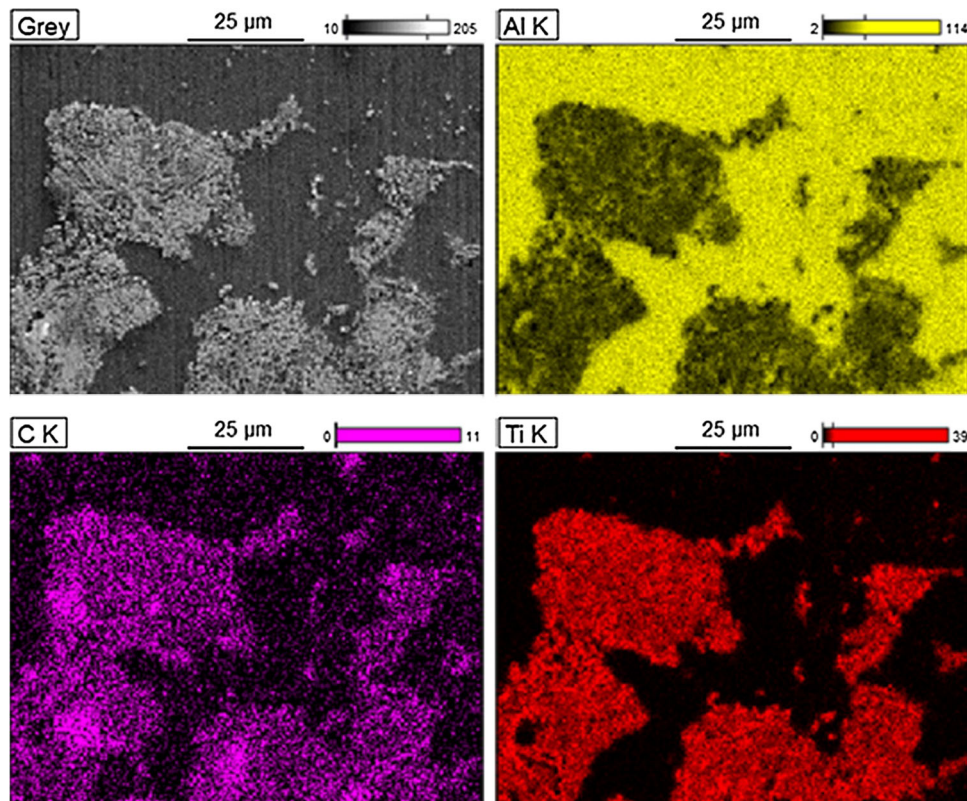


Fig. 15 EDS mapping of the worn surface on the Sample 3 at 15 N

EDS mapping results, it could be inferred that the investigated particles in Fig. 15 were identified as TiC according to the Ti and C elements distribution. The EDS results also agreed with the XPS analysis. Moreover, there were no SiC residual particles in the TiC_p region on the worn surface on the account of the TiC_p superior hardness. However, due to the soft Al matrix, a few SiC particles could be inlaid into the surface during the wear test.

The wear mechanism could be summarized as the abrasive and plowing wear between the contacting asperities of the coatings and the SiC sandpaper. When the wear load was low, the abrasion or cutting effect of SiC particles on the coating was not obvious. As the load increased, the depth of cutting or pressing into the coating by SiC abrasives became deeper, not only deepening the furrow left after cutting the coating by the SiC particles, but also producing spalling of more fragments. Furthermore, the TiC particles that peeled off from the coating also acted as the secondary wear particles.

4. Conclusions

In situ TiC_p/Al composite coating with 5 mm thickness was successfully fabricated on the aluminum substrate by a novel process of the SHS plus the V-EPC. It was verified that the SHS of the Ti-C system was realized with PTFE as an additive at a relatively low temperature of molten aluminum, which would benefit the cost-effective production of aluminum components with excellent wear resistance. The composite coating with 15 wt.% TP showed the optimal performance in terms of the hardness and wear resistance due to the uniform distribution of in situ 1-10 μm TiC hard particles. It was found via calculations

that with the same porosity, coarser produced TiC particles resulted in faster liquid aluminum infiltration. Through investigations on the friction and wear behavior of the composite coatings, it was illustrated that the wear mechanism of abrasion and plowing was predominant for all specimens, and less plowing and weight loss were observed at moderate amounts of TP.

Acknowledgments

This work was supported by the National Key R&D Program of China (Grant No. 2016YFB1101201) and the Fundamental Research Funds for the Central Universities (Grant No. FRF-TP-18-029A2). AAV acknowledges support from the National Science Foundation (IRES 1358088).

Conflict of interest

The authors declare that they have no conflict of interest.

Data Availability

The raw/processed data required to reproduce these findings are available from the corresponding authors upon reasonable request.

References

1. S. Katakam, N. Asiamah, S. Santhanakrishnan, and N. Dahotre, Laser In-Situ Synthesis of TiB₂-Al Composite Coating for Improved Wear Performance, *Surf. Coat. Technol.*, 2013, **236**, p 200–206

2. M. Magnania, P.H. Suegamaa, N. Espallargasb, S. Dostab, C.S. Fugivaraa, J.M. Guilemanyb, and A.V. Benedettia, Influence of HVOF Parameters on the Corrosion and Wear Resistance of WC-Co Coatings Sprayed on AA7050 T7, *Surf. Coat. Technol.*, 2008, **202**, p 4746–4757
3. O. Sarikaya, S. Anik, S. Aslanlar, S.C. Okumus, and E. Celik, Al-Si/B₄C Composite Coatings on Al-Si Substrate by Plasma Spray Technique, *Mater. Des.*, 2007, **28**, p 2443–2449
4. P.H. Gao, J.P. Li, Z. Yang, Y.C. Guo, and Y.R. Wang, Preparation of Al/SiC Composite Coatings on Surface of Aluminum Alloy by Atmospheric Plasma Spraying, *Rare Met. Mat. Eng.*, 2015, **44**, p 2396–2400
5. Z.X. Yang, A.H. Wang, Z.K. Weng, D.H. Xiong, B. Ye, and X.Y. Qi, Porosity Elimination and Heat Treatment of Diode Laser-Clad Homogeneous Coating on Cast Aluminum-Copper alloy, *Surf. Coat. Technol.*, 2017, **321**, p 26–35
6. S. Tomida and K. Nakata, Fe-Al Composite Layers on Aluminum Alloy Formed by Laser Surface Alloying with Iron Powder, *Surf. Coat. Technol.*, 2003, **174–175**, p 559–563
7. W.C. Gu, G.H. Lv, H. Chen, G.L. Chen, W.R. Feng, and S.Z. Yang, Characterisation of Ceramic Coatings Produced by Plasma Electrolytic Oxidation of Aluminum Alloy, *Mater. Sci. Eng. A*, 2007, **447**, p 158–162
8. U. Malayoglu, K.C. Tekin, U. Malayoglu, and S. Shrestha, An Investigation into the Mechanical and Tribological Properties of Plasma Electrolytic Oxidation and Hard-Anodized Coatings on 6082 Aluminum Alloy, *Mater. Sci. Eng. A*, 2011, **528**, p 7451–7460
9. J.H. Wang, M.H. Du, F.Z. Han., J. Yang, Effects of the Ratio of Anodic and Cathodic Currents on the Characteristics of Micro-arc Oxidation Ceramic Coatings on Al Alloys, *Appl. Surf. Sci.* 292 (2014) 658–664
10. H.R. Lashgari, M. Emamy, A. Razaghian, and A.A. Najimi, The Effect of Strontium on the Microstructure, Porosity and Tensile Properties of A356-10%B₄C Cast Composite, *Mater. Sci. Eng. A*, 2009, **517**, p 170–179
11. J. Hashim, L. Looney, and M.S.J. Hashmi, Metal Matrix Composites: Production by the Stir Casting Method, *J. Mater. Process. Technol.*, 1999, **92–93**, p 1–7
12. Y.C. Feng, L. Geng, P.Q. Zheng, Z.Z. Zheng, and G.S. Wang, Fabrication and Characteristic of Al-Based Hybrid Composite Reinforced with Tungsten Oxide Particle and Aluminum Borate Whisker by Squeeze Casting, *Mater. Des.*, 2008, **29**, p 2023–2026
13. X.X. Zhang, C.F. Deng, Y.B. Shen, D.Z. Wang, and L. Geng, Mechanical Properties of ABO₃+MWNTs/Al Hybrid Composites made by Squeeze Cast Technique, *Mater. Lett.*, 2007, **61**, p 3504–3506
14. K.B. Lee, H.S. Sim, S.Y. Cho, and H. Kwon, Reaction Products of Al-Mg/B₄C Composite Fabricated by Pressureless Infiltration Technique, *Mater. Sci. Eng. A*, 2001, **302**, p 227–234
15. A. Contreras, V.H. López, and E. Bedolla, Mg/TiC Composites Manufactured by Pressureless Melt Infiltration, *Scripta Mater.*, 2004, **51**, p 249–253
16. Z.Y. Liu, D. Kent, and G.B. Schaffer, Powder Injection Moulding of an Al–AlN Metal Matrix Composite, *Mater. Sci. Eng. A*, 2009, **513–514**, p 352–356
17. F. Ahmad, Orientation of Short Fibers in Powder Injection Molded Aluminum Matrix Composites, *J. Mater. Process. Technol.*, 2005, **169**, p 263–269
18. S. Mohammadkhani, E. Jajarmi, H. Nasiri, J. Vahdati-Khaki, and M. Haddad-Sabzevar, Applying FeAl Coating on the Low Carbon Steel Substrate Through Self-Propagation High Temperature Synthesis (SHS) Process, *Surf. Coat. Technol.*, 2016, **286**, p 383–387
19. J.Y. Xu, B.L. Zou, S.Y. Tao, M.X. Zhang, and X.Q. Cao, Fabrication and Properties of Al₂O₃-TiB₂-TiC/Al Metal Matrix Composite Coatings by Atmospheric Plasma Spraying of SHS Powders, *J. Alloys Compd.*, 2016, **672**, p 251–259
20. D. Siemiaszko and R. Mościcki, Kinetics Study on the SHS Reaction in Massive Samples with High Heating rate in the Fe–Al System, *J. Alloys Compd.*, 2015, **632**, p 335–342
21. M.A. Lagos, I. Agote, G. Atxaga, O. Adarraga, and L. Pambaguian, Fabrication and Characterization of Titanium Matrix Composites Obtained Using a Combination of Self Propagating High Temperature Synthesis and Spark Plasma Sintering, *Mater. Sci. Eng. A*, 2016, **655**, p 44–49
22. Q.Y. Hou, Microstructure and Wear Resistance of Steel Matrix Composite Coating Reinforced by Multiple Ceramic Particulates Using SHS Reaction of Al–TiO₂–B₂O₃ System During Plasma Transferred Arc Overlay Welding, *Surf. Coat. Technol.*, 2013, **226**, p 113–122
23. H. Jafari, M.H. Idris, and A. Shayganpour, Evaluation of Significant Manufacturing Parameters in Lost Foam Casting of Thin-Wall Al–Si–Cu Alloy Using Full Factorial Design of Experiment, *Trans. Nonferr. Metal. Soc.*, 2013, **23**, p 2843–2851
24. W. Jiang, Z. Fan, D. Liu, D. Liao, X. Dong, and X. Zong, Correlation of Microstructure with Mechanical Properties and Fracture Behavior of A356-T6 aluminum Alloy Fabricated by Expendable Pattern Shell Casting with Vacuum and Low-Pressure, Gravity Casting and Lost Foam Casting, *Mater. Sci. Eng. A*, 2013, **560**, p 396–403
25. T. Shi, L.C. Guo, J.J. Hao, C.G. Chen, J. Luo, and Z.M. Guo, Microstructure and Wear Resistance of In-Situ TiC Surface Composite Coating on Copper Matrix Synthesized by SHS and Vacuum-Expendable Pattern Casting, *Surf. Coat. Technol.*, 2017, **324**, p 288–297
26. T. Shi, Z.M. Guo, J.J. Hao, J. Luo, and J. Cheng, Reactive Cladding TiC-(Cr, Fe)7C3 High Manganese Steel Surface Reinforced Composite Materials, *Mater. Sci. Eng. Powder Metall.*, 2014, **19**, p 259–264
27. L.S. Abovyan, H.H. Nersisyan, S.L. Kharatyan, R. Orrù, R. Saiu, G. Cao, and D. Zedda, Synthesis of Alumina-Silicon Carbide Composites by chemically Activated Self-Propagating Reactions, *Ceram. Int.*, 2001, **27**, p 163–169
28. R. Licheri, R. Orrù, and G. Cao, Chemically-Activated Combustion Synthesis of TiC-Ti Composites, *Mater. Sci. Eng. A*, 2004, **367**, p 185–197
29. Y.X. Chen, Z.M. Lin, J.T. Li, J.S. Du, and S.L. Yang, PTFE, an Effective Additive on the Combustion Synthesis of Silicon Nitride, *J. Eur. Ceram. Soc.*, 2008, **28**, p 289–293
30. A.R. Zumachyan, S.L. Kharatyan, H.L. Khachatryan, and A.G. Kirakosyan, Self-Propagating High Temperature Synthesis of SiC-Cu and SiC-Al Cermets: Role of Chemical Activation, *Int. J. Refract. Met. H.*, 2011, **29**, p 250–255
31. S.G. Tabrizi, S.A. Sajjadi, A. Babakhani, and W. Lu, Influence of Spark Plasma Sintering and Subsequent Hot Rolling on Microstructure and Flexural Behavior of In-Situ TiB and TiC Reinforced Ti6Al4V Composite, *Mater. Sci. Eng. A*, 2015, **624**, p 271–278
32. Y. Mazaheri, M. Meratian, R. Emadi, and A.R. Najarian, Comparison of Microstructural and Mechanical Properties of Al-TiC, Al-B₄C and Al-TiC-B₄C Composites Prepared by Casting Techniques, *Mater. Sci. Eng. A*, 2013, **560**, p 278–287
33. T. Sun, X.Z. Wu, R. Wang, W.G. Li, and Q. Liu, First-Principles Study on the Adhesive Properties of Al/TiC Interfaces: Revisited, *Comput. Mater. Sci.*, 2017, **126**, p 108–120
34. S. Cudzilo and W.A. Trzcinski, Calorimetric Studies of Metal/Polytetrafluoroethylene Pyrolants, *Pol. J. Appl. Chem.*, 2001, **45**, p 25–32
35. A.G. Merzhanov, S.Y. Sharivker, Self-Propagating High-Temperature Synthesis of Carbides, Nitrides, and Borides, In: Y.G. Gogotsi, R.A. Andrievski (eds) *Materials Science of Carbides, Nitrides and Borides*, NATO Science Series (Series 3. High Technology), Springer, Dordrecht, 68 (1999) 205–222
36. C. Benoit, H. Ellen, K. Nikhil, V. Dominique, and D. Sylvain, TiC Nucleation/Growth Processes During SHS Reactions, *Powder Technol.*, 2005, **157**, p 92–99
37. Y.F. Yang, H.Y. Wang, R.Y. Zhao, Y.H. Liang, L. Zhan, Q.C. Jiang, Effects of C Particle Size on the Ignition and Combustion Characteristics of the SHS Reaction in the 20 wt.% Ni-Ti-C System, *J. Alloys Compd.* 460 (2008) 276–282
38. S.Y. Oh, J.A. Cornie, K.C. Russell, Wetting of Ceramic Particulates with Liquid Aluminum Alloys: Part I. Experimental Techniques, *Metall. Trans. A*, 20A (1989) 527–532
39. J.J. Zhang, J.M. Lee, Y.H. Cho, S.H. Kim, H.S. Yu, Fabrication of Aluminum Matrix Composites by Quick Spontaneous Infiltration Process Through Combustion Reaction of Al–Ti–B₄C–CuO Powder Mixtures in Molten Aluminum, *Scripta Mater.* 69 (2013) 45–48
40. B. Liu, X.J. Liu, M.J. Liu, and Z.Y. Zhao, Infiltration Mechanism in SiC_p/Aluminum Matrix Composite Prepared by Nonpressure, *Mater. Manuf. Proc.*, 2011, **26**, p 1339–1345
41. H.L. Yu, W. Zhang, H.M. Wang, X.C. Ji, Z.Y. Song, X.Y. Li, and B.S. Xu, In-Situ Synthesis of TiC/Ti Composite Coating by High Frequency Induction Cladding, *J. Alloys Compd.*, 2017, **701**, p 244–255

Publisher's Note Springer Nature remains neutral with regard to jurisdictional claims in published maps and institutional affiliations.